LANGMUIR

pubs.acs.org/Langmuir Article

Light-Induced Dynamic Control of Particle Motion in Fluid-Filled Microchannels

Joshua E. Kauffman,[§] Abhrajit Laskar,[§] Oleg E. Shklyaev, Anna C. Balazs,* and Ayusman Sen*

Cite This: *Langmuir* 2020, 36, 10022−10032 Read Online

ACCESS | Metrics & More | Article Recommendations | Supporting Information

ABSTRACT: The design of remotely programmable microfluidic systems with controlled fluid flow and particle transport is a significant challenge. Herein, we describe a system that harnesses the intrinsic thermal response of a fluid to spontaneously pump solutions and regulate the transport of immersed microparticles. Irradiating a silver-coated channel with ultraviolet (UV) light generates local convective vortexes, which, in addition to the externally imposed flow, can be used to guide particles along specific trajectories or to arrest their motion. The method provides the distinct advantage that the flow and the associated convective patterns can be dynamically altered by relocating the source of UV light. Moreover, the flow can be initiated and terminated "on-demand" by turning the light on or off.

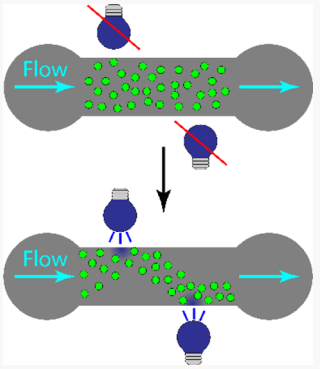

INTRODUCTION

With the increasing reliance of chemical industries on microscale devices for processing operations and the growing need for portable microfluidic systems, there is a push to create efficient microscopic platforms that can perform without extensive external machinery or complex setups.[1−6] It remains, however, a significant challenge to design microfluidic systems that enable fluid mixing or directed particle transport with minimal levels of external intervention. Ideally, these fluidic devices should exploit the inherent response of the enclosed solutions to an applied stimulus and thereby enable the fluid to amplify or augment the effects from the external cues.

Researchers have devised a range of effective methods for utilizing imposed flows or generating flows to controllably transport microscopic particles in microchannels.[7−12] In the case of imposed flows, the structure of microchambers can be tailored (e.g., by topographically patterning the inner walls[13,14]) to achieve the physical layout that is particularly useful for guiding particle motion. Patterning the charge distribution on a surface also permits control of electro-osmotic flow.[15] In the absence of imposed flows, the use of electric fields allows for controlled transport of charged particles in confined environments.[16,17] Other external sources of energy used to manipulate the spatio-temporal motion of microparticles inside fluid-filled microchannels[18] include acoustic[19,20] and magnetic fields.[21−23] The shortcoming of some of these methods is that the particles need to be modified to make them responsive to the applied stimuli. Acoustic propulsion requires special design of the channel geometry and the appropriate placement of the transducer to produce spatio-temporal pressure gradients.[24] The chemical energy from catalytic reactions has also been used to pump fluids and thereby drive the motion of particles to specified locations in the chamber.[25−29] In the current approach, the system is inherently responsive, i.e., the fluid responds to local heating by generating convective fluid flow. Consequently, the particles do not need to be altered, which is a significant advantage of the method. The mechanism of fluid motion generated through the coupling of light and heat[30−33] is general and can be applied to both nano- and microscopic particles and enables the sorting of heterogeneous mixtures of particles by size and density.[34] It is worth emphasizing that light provides a particularly useful means of manipulating flow since the stimulus can be applied remotely, patterned with a photomask, and readily translated to irradiate specified locations of the chamber. Herein, we describe a system that harnesses the intrinsic thermal response of a fluid to UV light to spontaneously pump the solution through the chamber and controllably transport the immersed microparticles. The method provides the distinct advantage that the flow and the associated convective patterns can be dynamically altered by relocating the source of UV light. Moreover, the flow can be initiated and terminated "on-demand" by turning the light on or off. Hence, the photothermal response of the fluid itself enables precise control over the functionality of the device.

Received: April 5, 2020
Revised: August 3, 2020
Published: August 7, 2020

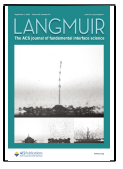

https://dx.doi.org/10.1021/acs.langmuir.0c00972
Langmuir 2020, 36, 10022−10032

To realize the above behavior, we consider a fluid-filled microchannel whose inner surfaces are coated with a thin film of silver. A UV light source located under the channel irradiates the silver; and the energy absorbed from the light is transduced into heat, which is transferred from the silver layer to the adjacent fluid. The heat gives rise to thermal buoyancy effects, where the less dense fluid rises to the top of the chamber and ultimately forms convective rolls (vortexes) that are centered about the beam of light. In addition to controlling the position and intensity of the light source, the flow pattern can be tailored by introducing an imposed flow, which ultimately determines the flow rate across the width of the channel. Hence, the combination of UV light and the imposed flow permits an effective means of controlling both the location of the convective vortexes and the rate of flow in the system. As we show below, this particular combination of factors provides a powerful means of regulating the spatial arrangement and motion of microparticles within the fluidic device. On a fundamental level, the studies also reveal how the interaction of convective and background flows affects the dynamics of the confined fluid.

Below, we first describe experimental methods and numerical techniques used to determine the flow fields produced by a combination of the thermal convection generated by UV light and externally imposed flow. We then use modeling to establish conditions where dynamically changing convective patterns could be harnessed to navigate cargo along a designated path in the channel or even arrest the particles propelled by the external pump.

EXPERIMENTAL METHODS

Microchannels were prepared using inspiration from traditional soft lithography techniques. Puffy Paint (iLoveToCreate, USA) was applied to a glass slide to create a template with cross sections of approximately 1 mm by 1 mm with up to 10% variation in each dimension. A Dow Sylgard 184 polydimethylsiloxane (PDMS) kit (1:10 curing ratio) was poured over the template to create the microchannel, which was, in turn, mounted on a glass slide. A solution (100 mM) of Tollen's reagent was injected into the channel, leading to spontaneous deposition of a continuous silver layer (~5 nm) on all surfaces. The channel was flushed with water to remove excess reagent after approximately 30 s. After flushing, the channel was washed with water multiple times to remove any remaining debris.

To induce a flow in the channel, a kd Scientific syringe pump was connected to the channel, and a solution of 3 μm carboxylate capped polystyrene tracer particles (PolyBead, USA) in water was pumped through at a variety of set flow rates. Note that small variations in background flow rates from that set on the pump are expected. Videos were collected on a Zeiss Axiovert 200 MAT microscope using a Point Grey Flea2 camera. Light was introduced into the system via a HAL 100 mercury arc lamp with a Chroma UV filter, which lowered the light intensity to roughly 32 mW/cm^2 at 320 nm with an irradiation spot of approximately 2 mm. Using a 1 cm light meter to read the intensity, we approximated an intensity of 785 mW/cm^2 for a 2 mm spot. The wavelength range of the light was limited to 300−400 nm. Tracer particles were tracked to determine fluid velocity using Tracker, a program produced by Open Source Physics. Data was exported into Microsoft Excel, and particle velocities were calculated using root-mean-square analysis.

Computational Methods. Similar to the experimental setup, we modeled a horizontal fluid-filled rectangular channel of length L_x = 10 mm, width L_y = 1 mm, and height L_z = 1 mm and assumed that a flow is imposed along the x direction from right to left. As displayed in Figure 1A, a beam of UV light is used to irradiate the bottom wall of the channel at the position x = 5 mm. For simplicity, the cross section of the incident beam is assumed to have a rectangular shape with dimensions 1 mm × 2 mm. The incident beam passes through the transparent glass

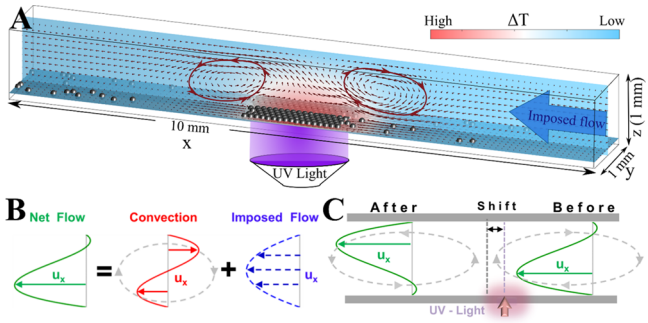

Figure 1. (A) Horizontal channel, coated inside with silver, irradiated with ultraviolet (UV) light in the presence of an imposed flow. A convective flow is generated above the heated region. The background color shows the temperature of the fluid, and the arrows show the direction of fluid flow. (B) Horizontal velocity (u_x) of the net flow (green) including contribution from a thermally generated convection (red) and externally imposed flow (blue). Convective vortexes are shown with gray. (C) Profile of the net flow changes from "before" to "after" the irradiated spot (violet). Shift indicates a displacement of the center of convective vortexes due to the imposed flow.

wall before hitting the metallic layer of silver, which coats the inner walls of the channel. The energy absorbed by the silver coating from UV light is transmitted to the fluid as heat. The heated fluid expands in volume, becomes less dense, and rises upward, while a colder fluid from the surroundings moves toward the irradiated spot and thereby creates thermally induced convective rolls. To elucidate factors controlling the heat-generated convection and transport of particles in the channel, we develop a theoretical model described below to simulate the behavior of the system and thereby predict how the combination of light and heat can be used to control both the fluid flow and particle motion inside the microchannel.

Given that T_0 is the ambient temperature of the external environment, the heat generated in the chamber raises the local temperature to the value T, and the corresponding change in the density of the fluid is captured through the expression $\Delta\rho = -\rho_0\beta_T(T - T_0)$, where ρ_0 is the density of the fluid at T_0 = 293 K, and $\beta_T = 207 \times 10^{-6}$ K^{-1} is the volumetric coefficient of thermal expansion. In the limit where variations in the density of the solution are relatively small, we can model the buoyancy-driven flow through the Boussinesq approximation of the Navier−Stokes equation

$$\frac{\partial \mathbf{u}}{\partial t} + (\mathbf{u}\cdot\nabla)\mathbf{u} = -\frac{1}{\rho_0}(\nabla p + \mathbf{F}_b + \mathbf{F}^{IB}) + \nu\nabla^2\mathbf{u} + \frac{\Delta\rho}{\rho_0}\mathbf{g};$$
$$\nabla\cdot\mathbf{u} = 0 \quad (1)$$

In this approximation, the density differences appear in the last term on the right-hand side of the equation, where $\Delta\rho$ is multiplied by the gravity vector $\mathbf{g}$. In other words, due to gravity, the local variations in mass per unit volume give rise to the fluid flow. The velocity of the flow is given by $\mathbf{u}$, and ν is the kinematic viscosity of the fluid.

The externally imposed flow is modeled as a uniform body force, $\mathbf{F}_b$, acting on the fluid along the x direction. $\mathbf{F}^{IB}$ represents forces originating from fluid-particle interactions and treated through the immersed boundary (IB) method.[35,36] We solve the Navier−Stokes equation and continuity equation (eq 1) using a lattice Boltzmann scheme,[37] in conjunction with no-slip boundary conditions for confining walls in the y and z directions (Figure 1) and periodic boundary conditions $\mathbf{u}|_{x=0} = \mathbf{u}|_{x=L_x}$ along the x direction.

The temporal evolution of the temperature within the confined fluid is

$$\frac{\partial T}{\partial t} + (\mathbf{u}\cdot\nabla)T = \alpha\nabla^2 T \quad (2)$$

where $\alpha = \kappa/c_p\rho_0$ is the thermal diffusivity, expressed in terms of the thermal conductivity of the solution κ, the constant density ρ_0, and the

https://dx.doi.org/10.1021/acs.langmuir.0c00972
Langmuir 2020, 36, 10022−10032

specific heat c_p. We prescribe the periodic boundary conditions for the temperature field along the x direction $T|_{x=0} = T|_{x=L_x}$, isothermal boundary conditions at the top wall $T|_{z=L_z} = T_0$, and zero heat flux conditions on the other walls $\partial T/\partial y|_{y=0} = \partial T/\partial y|_{y=L_y} = \partial T/\partial z|_{z=0} = 0$, except for the area irradiated by UV light. In the irradiated area, the silver coating constantly absorbs energy from UV light and transmits heat to the nearby fluid. Hence, the appropriate boundary condition describes a constant heat flux, $\frac{\partial T}{\partial n} = R$. Here, n is the local normal to the irradiated bottom wall of the channel. The magnitude of the heat flux into the fluid, R, depends on the geometry and size of the fluidic channel, material properties of the coating and the fluid, and the wavelength and the intensity of the incident UV radiation.[32,34] The size of the rectangular irradiated zone on the bottom is 1 mm × 2 mm. We adjust R in our model to match temperature variations observed in the experiments. A typical temperature rise due to the irradiation is $\Delta T = T - T_0 \approx 1$ K, and the corresponding value for R is 1.5×10^3 K/m.[32] We note that the periodic boundary conditions prescribed along the direction of the flow in the channel are valid when the effects of local heating by UV irradiation (and concurrent convective flows) have negligible contributions to the net flow close to the boundary. Therefore, the irradiation zones for different scenarios considered in this study are always kept far away from the periodic boundaries along the x direction. Also, simulating faster flows requires longer channels to reduce the effect of periodic images. The evolution equation for temperature (eq 2) is solved by a finite-difference scheme along with equations for the fluid dynamics (eq 1).

To study particle entrainment by the fluid flow, we consider N passive spheres of radius $a = 60$ μm submerged in the solution. The position vectors of the particles are $\mathbf{r}_i = (x_i, y_i, z_i)$ for all $i \in \{1, N\}$. Each of the submerged particles is modeled as a single node through the immersed boundary method,[35,36] and movements of the particles are simulated using the following equation

$$\frac{\partial \mathbf{r}_i}{\partial t} = \mathbf{u}(\mathbf{r}_i) \qquad 1 \le i,\ l \le N \tag{3}$$

where, $\mathbf{u}(\mathbf{r}_i)$ is the local fluid flow at each node point. Each particle is subject to the gravity force $\mathbf{F}_g^p = 4\pi a^3(\rho_m - \rho_0)\mathbf{g}/3$, directed downward along the gravity vector $\mathbf{g}$. The density of the particles is given by ρ_m. Each particle also experiences forces due to steric repulsion from the other particles, $\mathbf{F}^{PP}$, and from the sidewalls of the channel, $\mathbf{F}^{PW}$. The distance of the particle from the respective sidewall, W_n, is given by $\mathbf{r}_i - \mathbf{r}_i^{W_n}$. The forces describing the steric repulsion, $\mathbf{F}(\mathbf{r}) = -\partial U(r)/\partial \mathbf{r}$, are defined through the following Morse potential

$$U(r) = \begin{cases} \varepsilon(1 - \exp[-\omega(r - r_0)])^2 & r < r_0 \\ 0 & r \ge r_0 \end{cases} \tag{4}$$

Here, $r = |\mathbf{r}_i - \mathbf{r}_x|$ is the distance between the position of the ith particle and the repelling object $\mathbf{r}_x$ (another particle or wall). The strength and width of the potential are respectively denoted as ε and ω, and r_0 is the equilibrium (and cutoff) distance.

In the low Reynolds number regime realized in our model, effects of particle inertia can be neglected. To conserve momentum exchange between the particles and the fluid, the forces acting on each of the particle nodes are balanced by the hydrodynamic drag force, $\mathbf{F}^h = -(\mathbf{F}_g^p + \sum \mathbf{F}^{PP} + \sum \mathbf{F}^{PW})$. Following the immersed boundary procedure,[35,38] the force $\mathbf{F}^{IB} = -\sum \mathbf{F}^h$ is transmitted to the fluid in eq 1.

Below, we first compare the results of the above computational model and the corresponding experiments to calibrate and validate our modeling approach. We then use this validated approach to predict new phenomena involving particle transport within the channel that can be an impetus for future experimental studies.

RESULTS AND DISCUSSION

The net fluid flow in the microchamber illustrated in Figure 1A is due to effects from both the external pump and the thermally generated convection. In the absence of the externally imposed flow, the fluid convection can be explained as follows. The thin film of silver that coats the inner surfaces of the microchannel absorbs UV light emitted from the lamp located under the channel (Figure 1A). The energy associated with the absorption of light is transduced into heat, which is transferred from the silver layer to the adjacent fluid. The heat reduces the density of the local fluid and causes the more buoyant liquid to rise to the top of the channel. Due to the continuity of the fluid confined in the chamber, the less dense fluid is replaced by the more dense fluid at the bottom wall. When the warmer fluid reaches the top of the chamber, heat is transmitted to the top wall, causing the fluid to cool. The increased density of the cooler fluid causes the solution to sink to the bottom of the chamber. As a result, two counter-rotating convective vortexes (indicated with red closed loops and arrows) are created and localized approximately above the region irradiated with UV light, as shown in Figure 1A. Note that the horizontal component of the fluid velocity is equal to zero in the region between the vortexes. The thickness of the silver film (~5 nm) is much smaller than the wavelength of light, the channel dimensions, and the size of the tracer particles. Thus, small variations in film thickness do not have a significant effect on local heating and, in turn, the convective flows.

For convenience, flow at the bottom of the channel toward the illuminated region is called "inward" flow. The thermally generated inward flow and the convective vortexes can be harnessed to control the flow pattern within the microchamber. In particular, the convective flow depends on the position of the UV light beam, and hence, the flow patterns within the channel can be tailored through the appropriate arrangement of light sources.

The imposed flow from the external pump alters the dynamic behavior in the system. The center of the convective flow pattern is no longer directly above the UV light source; instead, the imposed flow pushes the convective center farther down the channel as the background flow rate is increased. The origin of the structure of the fluid flow within a channel for this scenario is shown schematically in Figure 1B and can be explained as follows. In the absence of UV light, the velocity field in the middle of the channel produced by external pumping has an approximately parabolic Poiseuille profile, shown schematically with blue dashed lines in Figure 1B. Profiles of the horizontal fluid velocities produced by the convective vortexes have an S-like shape (in the vertical section through the vortex center), as shown with the red lines. The combination of the two contributions produces a net flow with the velocity profiles shown with green lines in Figure 1B.

The velocity profiles of the net flow across the channel can be characterized into two regions: "before" and "after" the irradiated spot, as shown in Figure 1C. In the "before" region, the inward convective flow speeds up the imposed flow at the bottom half of the channel and slows down the imposed flow at the top half of the channel. Consequently, as shown in Figure 1C, the net fluid velocity profile in the "before" region becomes asymmetric, with high fluid velocity at the bottom half and slow fluid velocity at the top half. In contrast, in the "after" region, the convective flow slows down the imposed flow at the bottom half of the channel and speeds up the imposed flow at the top half of the channel, producing an asymmetric flow profile with low fluid velocity at the bottom half and high fluid velocity at the top half of the channel. Despite the asymmetric nature of the flow profile at different regions, the total amount of the fluid that flows through any cross section (in the y-z plane) of the channel is constant due to incompressibility of fluids. This constant rate of

https://dx.doi.org/10.1021/acs.langmuir.0c00972
Langmuir 2020, 36, 10022−10032

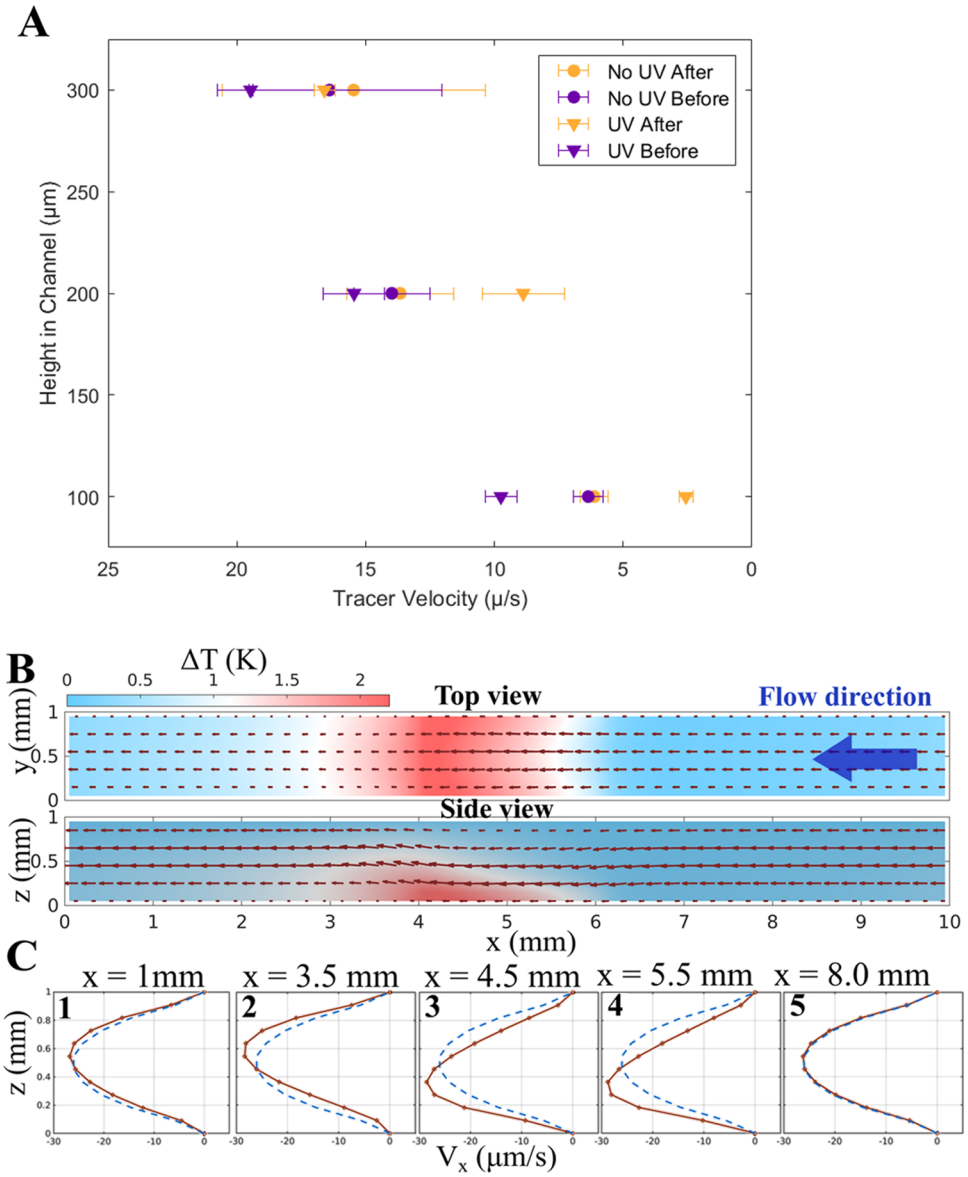

Figure 2. Thermal convection modifying the imposed Poiseuille flow. (A) Experimentally observed flow profiles in the middle section (y = 0.5 mm) in the bottom half of the channel. The syringe pump was set to impose a flow rate of 100 μL/h. Before the irradiation spot, convective flows amplify the background flow. After the spot, convective flows oppose the background flow. Fifteen tracers were tracked at a distance of 180 ± 10 μm before and after the irradiation point. Error bars are standard deviations of the average velocity. (B) Top (z = 0.2 mm) and side (y = 0.5 mm) views from the simulations with an imposed flow rate of 46 μL/h. A big blue arrow shows the direction of the imposed flow, and small red arrows indicate normalized magnitudes and directions of the flow. Red and blue background colors indicate hot and cold regions, respectively. (C1−5) Simulation results in panels showing velocities of the net flow (red solid line) in comparison to the imposed Poiseuille profile (blue dashed lines) for different x positions along the channel. The effect is prominent before and after (downstream) the irradiated spot (4 mm < x < 6 mm). Before UV corresponds to C4, while after UV occurs around C2. Negative signs of the x component of fluid velocities indicate that the fluid in the channel flows from the right to the left.

flow across any cross-sectional area of the channel is set by the external pump, and the Reynolds number for experimental data and the simulations is on the order of magnitude of 10^{-2}−10^{-1}.

Figure 2 shows results from both the experimental and computational studies that demonstrate the effect of convection on the distribution of velocities in the net flow throughout the channel. Figure 2A shows the velocity of tracer particles as functions of their distance from the bottom wall with an imposed background flow rate of 100 μL/h. The triangles show velocities of tracer particles tracked at distances of 130 ± 30 μm before and after the center of the irradiated spot. For comparison, tracer velocities without irradiation are shown with circles. Due to the complexity of the fluid flow around the irradiated region, tracer velocities at heights in the middle of the channel could not be reliably resolved in the experiment. Because the convective vortexes amplify the imposed flow before the UV light source and oppose the flow after the light source, the tracers in the respective regions move faster and slower, respectively, than in the control experiment. Control experiments conducted without irradiation have no fluid convection resulting in normal Poiseuille flow throughout the channel.

Figure 2B shows that the same dynamic behavior seen in the experiments is also observed in the simulations. The heat absorbed by the fluid from the irradiated spot (4 mm < x < 6 mm) on the bottom wall is indicated by an increase in temperature, as marked in red in the top and side views of the

https://dx.doi.org/10.1021/acs.langmuir.0c00972
Langmuir 2020, 36, 10022−10032

channel. The red arrows show fluid velocities that have contributions from both thermally driven convection and the externally imposed flow. The shift between the center of the heated spot (5 mm) and maximal variations in the flow velocities (4 mm) can be seen in the side view of Figure 2B and is a consequence of external pumping driving the fluid from right to left. The magnitude of the shift depends on the rate of the imposed flow. Note that matching the simulated flow profile with that observed experimentally entailed using a slightly lower flow rate in simulations compared to the externally imposed flow rate in the experiments (46 μL/h versus 100 μL/h). We ascribe the difference to variations in the cross section of the experimentally fabricated channels and deviations in the background flow rates from that set on the pump (see the experimental section).

The fluid velocities obtained from the simulations for cases with (red solid line) and without (blue dashed line) irradiation with UV light are shown in Figures 2C1−5. To demonstrate the differences between the two cases, we plot the x component of the fluid velocities across the channel for different x positions. In the absence of any UV irradiation, the resulting Poiseuille flow has an approximately parabolic velocity profile. For the planes x = 4.5 mm and x = 5.5 mm located before the center of convective vortexes (displayed in Figures 2C3,4 and 3), we observe that the fluid close to the bottom wall of the channel moves faster than near the top wall, indicating the absence of the up-down symmetry that characterizes the Poiseuille flow. This feature in the flow is reversed just after the center of convective vortexes, which is located around x = 4 mm in this case. The flow profile at the x = 3.5 mm plane reveals that the fluid above the centerline (z > 0.5 mm) of the channel moves relatively faster, whereas the fluid below the centerline moves slower. Sufficiently far from the heated central region (x = 5 mm), i.e., at sections x = 1 mm and x = 8 mm, the flow velocities approach the parabolic profiles typical for Poiseuille flow.

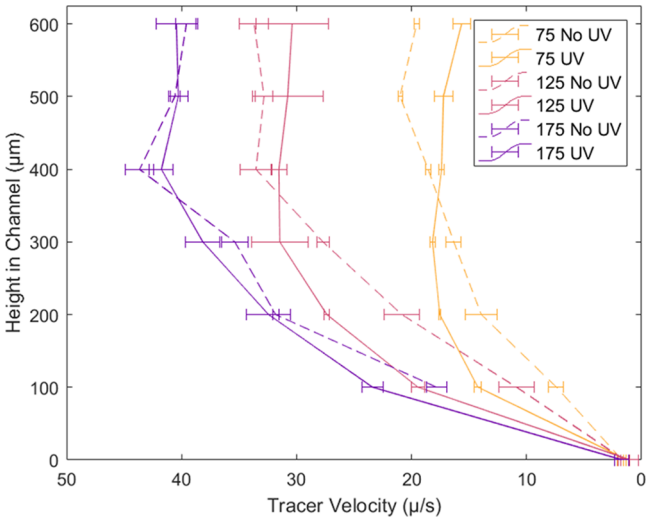

Figure 3. Flow profiles observed in the channel for background flow rates of 75 (yellow), 125 (pink), and 175 (purple) μL/h, with (solid lines) and without (dashed lines) irradiation with UV light. As the background flow rate increases, the relative convective effects are minimized. Control experiments are labeled No UV and consist of only a background flow. Fifteen tracers were tracked to obtain the fluid velocity at a distance of 160 ± 30 μm (x coordinate) before the center of the irradiation point and a y value of 500 ± 150 μm (channel width ≈ 1 mm). Error bars are the standard deviations of the average velocities.

Simulation results presented in Figure 2B agree qualitatively with the experimental results shown in Figure 2A. In particular, the "Before" UV line shown in Figure 2A corresponds to the C4 panel in Figure 2C, while the "After" UV line occurs around the panel C2. Consistent with the experiments, the simulations demonstrate that at the bottom wall (z = 0 plane), the additional convective flow accelerates the fluid before the irradiated spot and slows it after the heated spot. Simultaneously, at the top wall (z = 1 mm plane), the convection accelerates the flow after the irradiated spot and slows it down before the heated region of the channel. This behavior is a result of the conservation of the fluid flux across the channel that is controlled by the external pump.

To better understand the nature of the interactions between the background flow and the thermally induced convection, flow profiles for increasing background flow rates of 75, 125, and 175 μL/h were analyzed experimentally. Horizontal fluid velocities in the bottom half (below 600 μm) of the channel are plotted in Figure 3 for situations with (solid lines) and without (dashed lines) UV light. All measurements were taken at a distance 160 ± 30 μm before the irradiation point (which roughly corresponds to the position x = 5.5 mm and the inset C4 in Figure 2C) where the convective flow moves the fluid at the bottom of the channel in the same direction as the background flow. Note that while the velocities of the background flow are controlled by the external pump, velocities of the thermally driven flow are determined by the amount of heat generated under irradiation and remain the same for all experimental trials.

Flow profiles observed for flow rates presented in Figure 3 are qualitatively similar to one another and to the profiles in Figure 2A. A comparison between the profiles for 75 and 175 μL/h at a height of 200 μm reveals that at a higher flow rate (175 μL/h), the net flow (solid line) is almost the same as the imposed background flow (dashed line), thus indicating a relatively small contribution of the convective flow. At a lower flow rate (75 μL/h), however, we observe similar contributions of the background (dashed line) and convective components (difference between solid and dashed lines) to the net flow (solid line). In particular, at a height of 200 μm, the thermally generated convection increases flow velocities from ∼10−13 μm/s, provided by the background flow (dashed line) alone, to about ∼17 μm/s in the net flow (solid lines). Note that the influence of the convective flow on the net flow remains significant only in the proximity of the irradiated region and decays to zero away from that region. This decay can also be seen in the simulation results in Figure 2C, which shows the velocity profiles at different x locations along the channel. The profiles of the fluid flows depend on the distance from the irradiated region. The total amount of fluid that flows across any cross section of the channel, however, remains constant due to incompressibility of the fluid and is set by the flow rate imposed by the external pump.

In the experiments, the velocities of the fluid at heights beyond the z = 0.6 mm plane are difficult to test due to limitations of the experimental setup. Below the z = 0.6 mm plane, the flow profiles before the illuminated region demonstrate an increase of the net flow by the thermally driven convection. It is also difficult to measure the fluid flow experimentally in the "after" region due to the shift in the convective center.

The analysis of the flow velocity profiles presented in Figures 1−3 suggests that the effect of the convective flow due to local heating on the imposed fluid flow decreases as the rate of the

https://dx.doi.org/10.1021/acs.langmuir.0c00972
Langmuir 2020, 36, 10022−10032

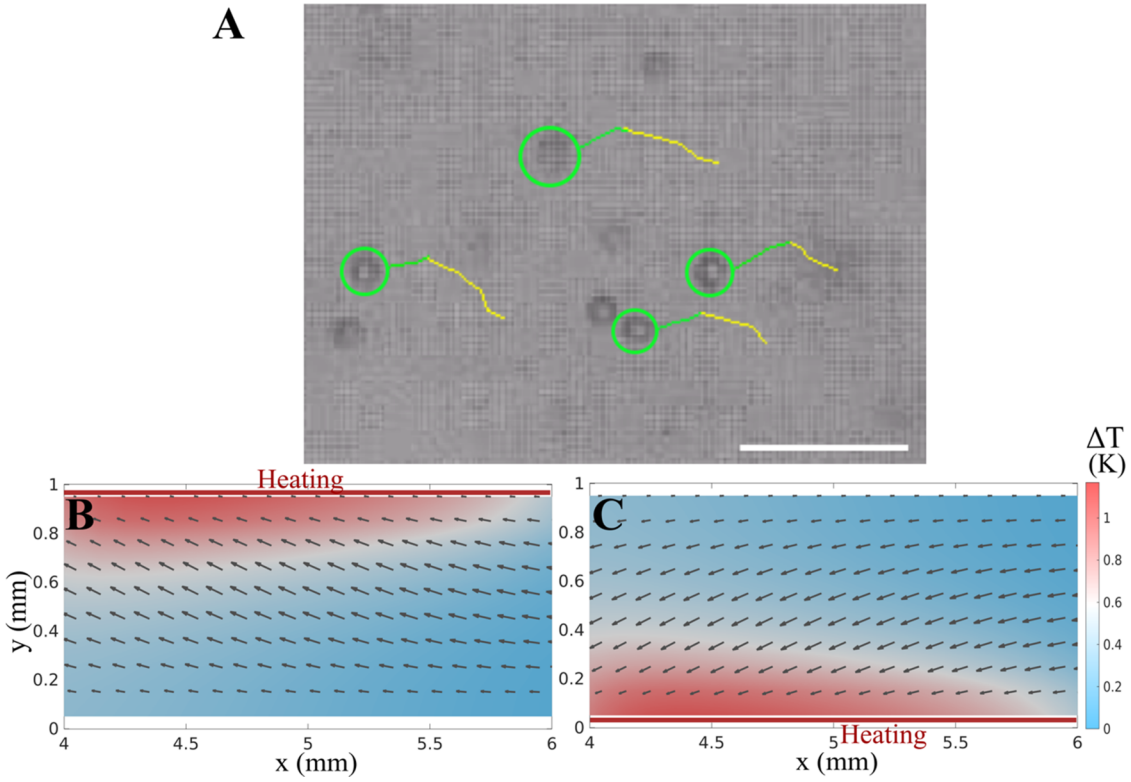

Figure 4. Change in the direction of flow caused by the relocation of UV light as shown in Supplemental Video 1. (A) Tracks of particles (3 μm diameter) before and after a shift in the UV light position on the bottom surface. Yellow tracks show particle motion when UV light is focused at the top left of the frame, while green tracks show the trajectory change after UV light is moved to the bottom left of the frame. A background flow of 75 μL/h was controlled with a syringe pump. The scale bar is 20 μm. The x and z coordinates remain the same during the experiment, but the y coordinate of the light spot is moved from ~500 μm (yellow line) to ~800 μm (green line). We define the coordinates as follows: The x direction is defined as the length of the channel, the y direction is the width of the channel, and the z direction is the height of the channel. (B,C) Simulated flow lines at height 0.1 mm. The red areas represent regions heated with UV light. The increased temperature is shown with a red color. The rate of the imposed flow in the simulation is Q = 23 μL/h. The small red arrows indicate normalized magnitudes and directions of the flow.

imposed flow increases. The effect of the convective flow is the highest when there is little imposed flow. As the imposed flow rate is increased, the relative contribution of the convection into the resulting (combined) field of fluid velocities decreases. Because the heating rate is fixed by the design of the channel and the UV light source, the effect of convection is larger for a background flow rate of 75 μL/h compared to a background flow rate 200 μL/h. The absorption of UV irradiation by the metallic layer and the release of heat to the solution depend on the properties of the metallic coating and overall geometry of the channel. The net fluid flow through the channel is conserved and is controlled solely by the imposed flow rate and not by the convective flow due to local heating. The convective flow generated by UV irradiation modifies the Poiseuille flow profile as described in Figure 1 (without modifying the net flow rate) and patterns the flow in three dimensions. We will explore this phenomenon in the next section to design novel particle trajectories inside a microchannel.

Particle Transport Controlled by UV Light. A particularly useful feature of the system is the ability to control the trajectories of particles transported along the channel. In a previous report,[32] the repositioning of the beam of UV light caused a shift of the convective pattern generated by the light and concurrent relocation of a cluster of particles aggregated on the bottom of the fluidic chamber. In the system considered here, by relocating UV light, we can control the speed and the direction of the net flow locally within a channel. To demonstrate such control over the flow, we fix a background flow rate of 75 μL/h and consider the motion of the tracer particles at approximately 100 μm off the bottom surface. Figure 4A (and Supplemental Video 1) shows that when UV light is focused at the top left portion of the viewing area, the tracer particles move toward the irradiated spot due to influence from both the convective and imposed flows. When the light is shifted to the bottom left of the viewing area, the fluid, together with the submerged tracers, moves in that direction.

Qualitatively similar patterns of fluid flow are obtained in the simulations. In particular, a section (4 mm < x < 6 mm) of the sidewall at y = 1 mm is first irradiated with UV light (see Figure 4B). Then, the irradiation spot is shifted to the other sidewall at y = 0 mm (see Figure 4C). In the top-down views, the heated sidewalls are demarcated by red lines at the top and at the bottom of the viewing area. The convection-driven fluid flows toward the sidewall, at y = 1 mm, along the bottom surface of the channel as the same sidewall is heated with irradiation (Figure 4B). As the irradiation spot is relocated to the bottom sidewall, at y = 0 mm, the direction of the flow changes direction toward the bottom sidewall (Figure 4C). The change of direction of the flow at the z = 0.1 mm plane is shown with black arrows in panels 4B and 4C. The backgrounds of the panels are pseudo-colored with corresponding temperature map. The red and blue colors indicate regions of high and low temperatures, respectively.

The general agreement between the results from the experiments and simulations in these studies provides a

https://dx.doi.org/10.1021/acs.langmuir.0c00972
Langmuir 2020, 36, 10022−10032

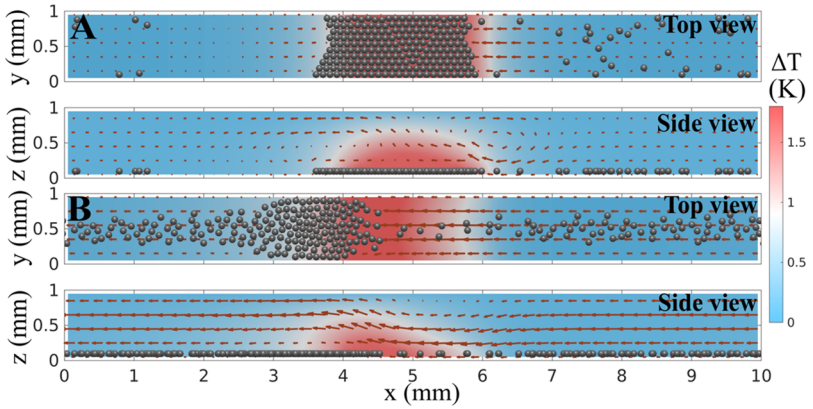

Figure 5. Influence of a single heat source on particle transport. The increased temperature measured in units of Kelvin is shown in red. (A) Thermally generated convection dominating the imposed flow (4.6 μL/h) and aggregating 400 particles (a = 60 μm) into a cluster (Supplemental Video 2). (B) Imposed flow of intermediate strength (23 μL/h) dragging particles along a central line (where the flow is faster) on the bottom wall (Supplemental Video 3). The irradiated spot is below the bottom surface between 4 and 6 mm. The small red arrows indicate normalized magnitudes and directions of the flow.

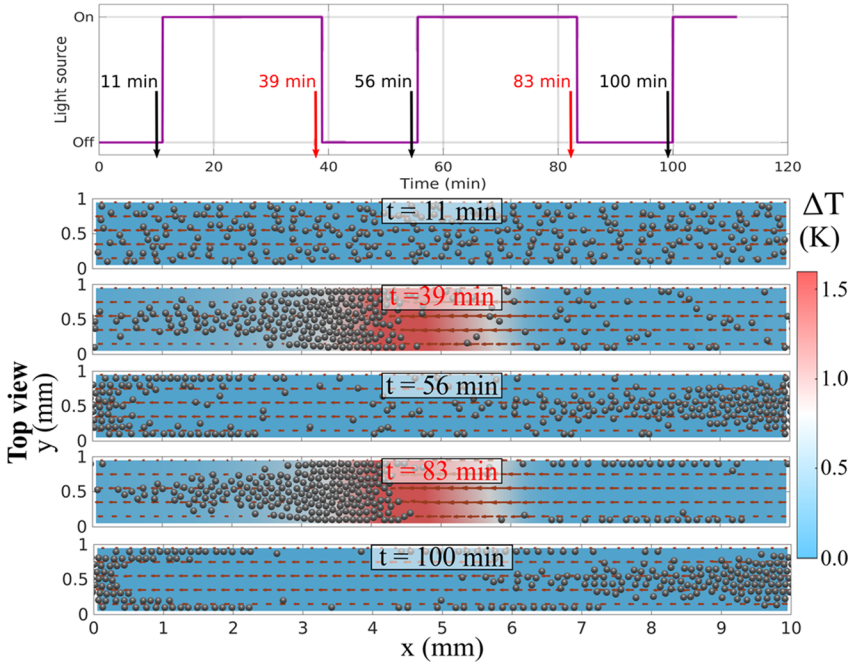

Figure 6. Control of particle traffic by periodic heating of the bottom wall of the channel (4 mm < x < 6 mm) with UV light (Supplemental Video 4). The increased temperature measured in units of Kelvin is shown in red. The time-dependent irradiation signal is shown in the top panel. Simulation snapshots in the lower panels demonstrate particle migration when the light is off and partial arrest around the heated zone when the light is on. The rate of the imposed flow Q = 23 μL/h. The small red arrows indicate normalized magnitudes and directions of the flow.

validation of our computational approach. Using this validated approach, we utilize our simulations to predict how the dynamic relocation of the heat sources (irradiated regions) can be used to control, guide, and arrest the motion of microparticles carried by the imposed flow along the microchannel. We first describe the effect of a single source of UV light on the externally imposed flow, and then, we discuss the entrainment of particles within a chamber that is heated by multiple light sources.

The convective flow produced by a single UV light source is shown in Figure 5, where the microparticles in the solution are trapped around the irradiated spot (panel A) and entrained along a central line on the bottom wall of the channel (panel B). The particles are initially uniformly dispersed in the solution but sediment to the bottom wall due to gravity and are dragged by the net fluid flow, which has contributions from both the convective and imposed flows. For a relatively weak imposed flow (or strong convection), shown in Figure 5A and Supplemental Video 2, the convective vortexes around the irradiated spot dominate and drag the particles toward the center of the irradiated hot spot. These particles eventually aggregate into a cluster. For an imposed flow of intermediate strength, shown in Figure 5B and Supplemental Video 3, the convective flow traps the particles at the edges (y = 0 and y = 1 mm) of the irradiated zone only. The particles are slowed down at the left end of the irradiated zone because the net flow moves from right to left. The convective flow, however, cannot completely arrest the particles around the central line (y = 0.5 mm) of the bottom of the channel, where the imposed Poiseuille flow has higher fluid velocities than at the edges (y = 0 and y = 1 mm). Consequently, particles carried by the flow form a

https://dx.doi.org/10.1021/acs.langmuir.0c00972
Langmuir 2020, 36, 10022−10032

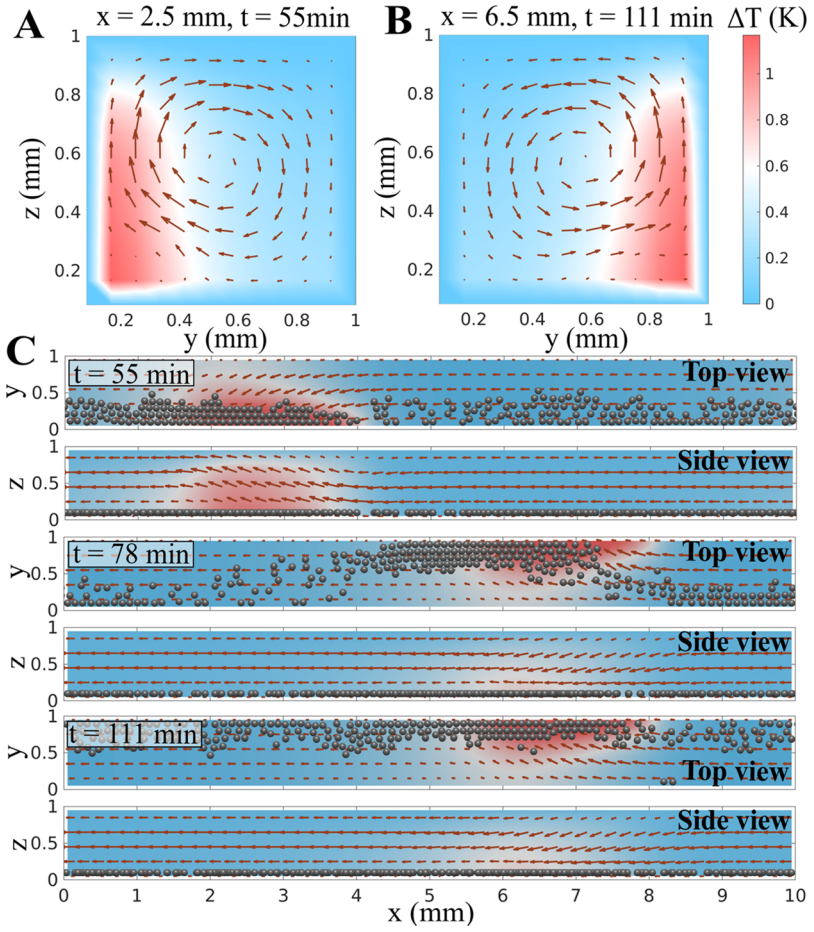

Figure 7. Control of the particle trajectories by a single irradiation source on the sidewalls of the channel. (A) Heating of the left wall generating a vortex (in the *y*-*z* plane at $x = 2.5$ mm) shown with red arrows, which drags particles to the left. (B) Heating of the right wall generating a vortex (in the *y*-*z* plane at $x = 6.5$ mm) that drags particles to the right. (C) Sequence of top and side views illustrating a dynamic relocation of the heat source, which changes the particle trajectories (Supplemental Video 5). Irradiation of the left wall (2 mm < x < 4 mm and $y = 0$ mm) for the initial 56 min promotes particle transport along the left bottom corner. Shifting the light to the right wall (6 mm < x < 8 mm and $y = 1$ mm) after initial irradiation induces transition to the particle transport along the right bottom corner (shown at $t = 78$ min). At $t = 111$ min, most of the particles move along the right bottom corner of the channel. The rate of the imposed flow $Q = 23$ μL/h. The small red arrows indicate normalized magnitudes and directions of the flow.

continuous stream through the center of the bottom wall of the channel as shown in Figure 5B.

The trapping of particles by the convective flow can be used to control the transport of particles along the channel much like a traffic signal regulating traffic on a street. To demonstrate this behavior, we irradiate the bottom wall (within 4 mm < x < 6 mm) of the channel periodically in time (Figure 6 and Supplemental Video 4). The top panel in Figure 6 shows the state of the UV light signal as a function of time. The snapshots from the simulation in the bottom panels demonstrate the spatial and temporal control over particle traffic. Initially, the uniformly dispersed particles sediment to the bottom wall while being carried by the flow along the channel. When the light is on ($t = 39$ min), the convective flow traps the particles (as in Figure 5B) at the edges ($y = 0$ and $y = 1$ mm) near the left end of the heated zone (4 mm < x < 6 mm) in the channel. Some particles, however, are moved through the central line ($y = 0.5$ mm) of the channel where the imposed flow has larger velocities. After the irradiation is switched off, the whole cluster of particles is driven downward by the imposed flow (shown at $t = 56$ min). The repetition of the particle entrapment into a cluster around the heated zone when the light is on ($t = 83$ min) followed by particle release when the light is off ($t = 100$ min) highlights the robust spatio-temporal control of particle traffic by irradiation.

Additional control over the particle trajectories can be obtained if specific regions on the vertical sidewalls of the channel are irradiated with light. In particular, the simulation results in the panels of Figure 7A,B demonstrate that heating either of the vertical sidewalls generates convective vortexes in the plane perpendicular to the x axis of the channel. The vortexes drag particles along the bottom toward the respective sidewalls, and hence, these vortexes provide an effective means to manipulate the particle trajectories. The image in Figure 4A from the experimental studies also indicates that the convective flow drags particles toward the illuminated sidewall. A sequence of top and side images in Figure 7C provides further details of the particle trajectories (Supplemental Video 5). Heating a region on the left sidewall (between 2 mm < x < 4 mm) for 56 min establishes the particle transport along the left bottom corner ($z = 0$ and $y = 0$ mm). Shifting the heated region to the right wall (between $6 \leq x \leq 8$ mm) induces the transition of the particle trajectories from the left to the right wall. Eventually, all the particles are transported along the right bottom corner ($z = 0$ and $y = 1$ mm) of the channel.

https://dx.doi.org/10.1021/acs.langmuir.0c00972
Langmuir 2020, 36, 10022−10032

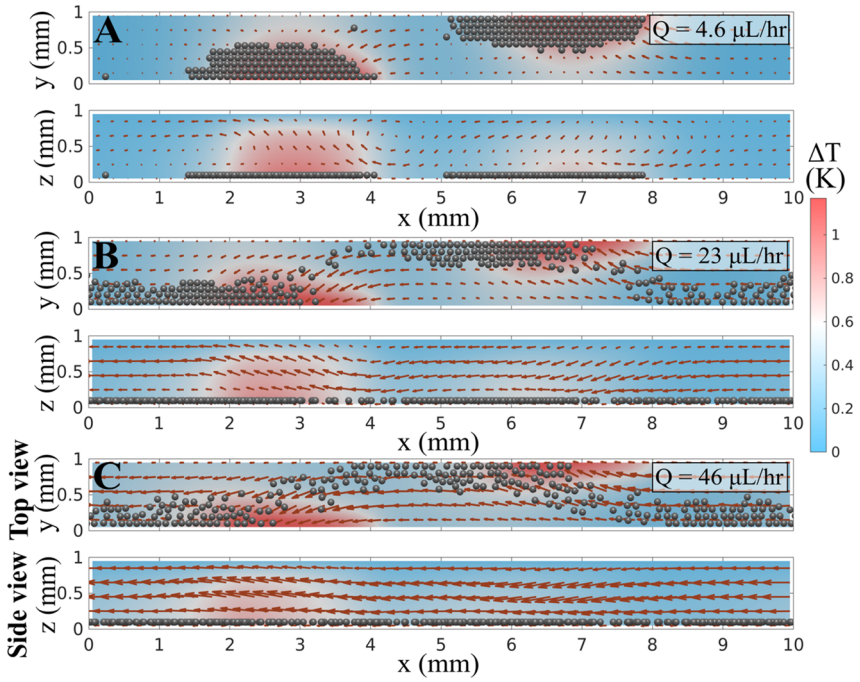

Figure 8. Control of the particle trajectories by two irradiation sources, which heat regions on the opposite sides of the channel located at 2 mm < x < 4 mm and y = 0 mm and 6 mm < x < 8 mm and y = 1 mm (Supplemental Video 6). The increased temperature is shown with a red color. Red arrows show the directions of the fluid flows. (A) At the rate of the imposed flow Q = 4.6 μL/h, the particles assembling in clusters above the heated regions. (B) At rate Q = 23 μL/h, the particles passing from one to another cluster. (C) At rate Q = 46 μL/h, the particle moving along serpentine trajectories. The small red arrows indicate normalized magnitudes and directions of the flow.

More complex particle trajectories can be designed by applying a number of light sources, which heat different regions of the channel. In the simulations (Figure 8 and Supplemental Video 6), we simultaneously heat two regions located on the left sidewall between x = 2 and 4 mm and on the right sidewall between x = 6 and 8 mm. The heating generates convective vortexes that drag particles toward the two regions. When the fluid flow generated by the external pump is slow in comparison to the thermally driven convective flow (panel A in Figure 8), the particles are trapped on top of the respective irradiated spots and form two separate islands. With an increase in the rate of the imposed flow, the islands start losing particles downstream as it is shown in panel B of Figure 8. Finally, at a relatively high rate of the imposed flow, the particles are dragged along the channel, and the convective vortexes are unable to localize the particle, as shown in panel C. The transported particles are moved down the stream by the imposed flow, which is spatially modulated by the convective flows associated with the heated regions. As a result, the particle trajectories assume a serpentine nature as they pass between the sidewalls along the bottom of the channel.

We note that the presence of walls with no-slip boundary conditions alters the flow profile and has significant effects on the particle motion. The scenario we considered in this work belongs to a low Reynolds number; therefore, the velocities of the imposed and convective flows can be combined. The imposed flow produces a Poiseuille profile with a peak, at $z = h/2$, at the center of the cross section of the channel. The convective flows form vortexes localized around the hot spot. The convective vortexes produce an "S"-like profile, which has the highest inward flow at $z = h/4$ and highest outward flow at $z = 3h/4$. The combined flow is shown schematically in Figure 1B,C with green lines. Such a flow profile affects the motion of the particles depending on their size. As the size of the particle becomes smaller, it will experience a smaller drag force from the fluid and, consequently, will need a longer time to migrate above the bottom surface. The no-slip boundaries at the sidewalls also affect the particle motion. In Figures 5 and 6, the particles at the corners of the channel, where sidewalls meet the bottom wall, move very slowly compared to particles located at the middle of the bottom wall. This is due to the Poiseuille flow profile, which has the highest velocity at y = 0.5 mm and zero at the two sidewalls of the channel, y = 0 and y = 1 mm. Consequently, the particles are trapped at the edge of the channel, and the particle islands lose particles through the middle section of the channel.

CONCLUSIONS

In summary, we show that irradiating a silver-coated channel with external UV light is an effective way to control particle migration and entrapment inside the fluidic environment of a microchannel. In particular, the heat released by irradiation with UV light generates local convective vortexes, which, in addition to the externally imposed flow, can be used to guide particles along specific trajectories or to arrest their motion. The combination of convective and background flows also changes the fluid dynamics in the channel with regions demonstrating local velocity increase and decrease. Positions of these regions can be changed simply by moving the UV light source, which, in turn, moves the convective center and causes particle and fluid motion toward the new convective center.

In addition to control over fluid dynamics, particles can also be entrapped and released using UV light. The principles of the particle manipulations within a microchannel are demonstrated through the application of one or two time-dependent UV light sources that enable complex spatio-temporal behavior of particles. Temporal modulation of UV light can enable particle transport with time-dependent velocities, with particles trapped

https://dx.doi.org/10.1021/acs.langmuir.0c00972
Langmuir 2020, 36, 10022−10032

and released on demand. More specifically, when convection dominates over background flow, particles can be trapped at the convective center, and when the UV light source is turned off, particles are released and move down the channel. A spatial organization of the light-heated regions inside the channel allows the guiding of particles along predesigned trajectories as they are dragged by the flow. While other heat sources could also be used to control particle transport, the advantage of light sources lies in greater flexibility due to easy relocation of the sources to new positions in the channel. In addition to manipulating passive particles transported by the net fluid flow, the described technique can be extended to manipulate self-propelling particles[38] or rheotaxing rods[39] along microfluidic channels.

■ ASSOCIATED CONTENT

Supporting Information

The Supporting Information is available free of charge at https://pubs.acs.org/doi/10.1021/acs.langmuir.0c00972.

Descriptions of the supporting videos (PDF)

Shifting the position of the UV light changes the background flow direction (AVI)

Thermally generated convection dominating the weak imposed flow (4.6 μL/h) and aggregating 400 particles (a = 60 μm) into a cluster (AVI)

Imposed flow of intermediate strength (23 μL/h) dragging particles along the central line (where the flow is faster) on the bottom wall (AVI)

Spatio-temporal control of particle motion by periodic heating of the bottom wall of the channel with UV light (AVI)

Control of the particle trajectories by a single irradiation source on the sidewalls of the channel (AVI)

Control of the particle trajectories by two irradiation sources that heat regions on the opposite sides of the channel (AVI)

■ AUTHOR INFORMATION

Corresponding Authors

Anna C. Balazs − *Department of Chemical and Petroleum Engineering, University of Pittsburgh, Pittsburgh, Pennsylvania 15261, United States;* orcid.org/0000-0002-5555-2692; Email: balazs@pitt.edu

Ayusman Sen − *Department of Chemistry, Pennsylvania State University, University Park, Pennsylvania 16802, United States;* orcid.org/0000-0002-0556-9509; Email: asen@psu.edu

Authors

Joshua E. Kauffman − *Department of Chemistry, Pennsylvania State University, University Park, Pennsylvania 16802, United States*

Abhrajit Laskar − *Department of Chemical and Petroleum Engineering, University of Pittsburgh, Pittsburgh, Pennsylvania 15261, United States;* orcid.org/0000-0003-2130-5607

Oleg E. Shklyaev − *Department of Chemical and Petroleum Engineering, University of Pittsburgh, Pittsburgh, Pennsylvania 15261, United States*

Complete contact information is available at: https://pubs.acs.org/10.1021/acs.langmuir.0c00972

Author Contributions

§J.E.K. and A.L. contributed equally to this work. All authors designed the system described here and determined the studies to be performed. J.E.K. conducted the experiments, and A. L. and O.E.S. performed the simulations.

Notes

The authors declare no competing financial interest.

■ ACKNOWLEDGMENTS

The authors gratefully acknowledge funding from NSF grant 1740630: CCI Phase I: Center for Chemomechanical Assembly. We also thank Benjamin Tansi for helpful discussions.

■ REFERENCES

(1) Good, B. T.; Bowman, C. N.; Davis, R. H. An effervescent reaction micropump for portable microfluidic systems. *Lab Chip* **2006**, *6*, 659−666.

(2) Gomollón-Bel, F. Ten Chemical Innovations That Will Change Our World: IUPAC identifies emerging technologies in Chemistry with potential to make our planet more sustainable. *Chem. Int.* **2019**, *41*, 12−17.

(3) Chang, C.-C.; Yang, R.-J. Electrokinetic mixing in microfluidic systems. *Microfluid. Nanofluid.* **2007**, *3*, 501−525.

(4) Whitesides, G. M. The origins and the future of microfluidics. *Nature* **2006**, *442*, 368−373.

(5) Boyd-Moss, M.; Baratchi, S.; Di Venere, M.; Khoshmanesh, K. Self-contained microfluidic systems: a review. *Lab Chip* **2016**, *16*, 3177−3192.

(6) Chen, C.; Mehl, B. T.; Munshi, A. S.; Townsend, A. D.; Spence, D. M.; Martin, R. S. 3D-printed microfluidic devices: fabrication, advantages and limitations—a mini review. *Anal. Methods* **2016**, *8*, 6005−6012.

(7) Kar, A.; Chiang, T.-Y.; Ortiz Rivera, I.; Sen, A.; Velegol, D. Enhanced Transport into and out of Dead-End Pores. *ACS Nano* **2015**, *9*, 746−753.

(8) Mou, F.; Zhang, J.; Wu, Z.; Du, S.; Zhang, Z.; Xu, L.; Guan, J. Phototactic Flocking of Photochemical Micromotors. *iScience* **2019**, *19*, 415−424.

(9) Karbalaei, A.; Kumar, R.; Cho, H. J. Thermocapillarity in Microfluidics-A Review. *Micromachines* **2016**, *7*, 13.

(10) Shin, S.; Um, E.; Sabass, B.; Ault, J. T.; Rahimi, M.; Warren, P. B.; Stone, H. A. Size-dependent control of colloid transport via solute gradients in dead-end channels. *Proc. Natl. Acad. Sci.* **2016**, *113*, 257−261.

(11) Marmottant, P.; Hilgenfeldt, S. A bubble-driven microfluidic transport element for bioengineering. *Proc. Natl. Acad. Sci. U. S. A.* **2004**, *101*, 9523.

(12) Maiti, S.; Shklyaev, O. E.; Balazs, A. C.; Sen, A. Self-Organization of Fluids in a Multienzymatic Pump System. *Langmuir* **2019**, *35*, 3724−3732.

(13) Kim, S. M.; Lee, S. H.; Suh, K. Y. Cell research with physically modified microfluidic channels: A review. *Lab Chip* **2008**, *8*, 1015−1023.

(14) Stone, H. A.; Stroock, A. D.; Ajdari, A. Engineering Flows in Small Devices: Microfluidics Toward a Lab-on-a-Chip. *Annu. Rev. Fluid Mech.* **2004**, *36*, 381−411.

(15) Stroock, A. D.; Weck, M.; Chiu, D. T.; Huck, W. T. S.; Kenis, P. J. A.; Ismagilov, R. F.; Whitesides, G. M. Patterning Electro-osmotic Flow with Patterned Surface Charge. *Phys. Rev. Lett.* **2000**, *84*, 3314−3317.

(16) Islam, N.; Wu, J. Microfluidic transport by AC electroosmosis. *J. Phys.: Conf. Ser.* **2006**, *34*, 356−361.

(17) Ai, Y.; Park, S.; Zhu, J.; Xuan, X.; Beskok, A.; Qian, S. DC Electrokinetic Particle Transport in an L-Shaped Microchannel. *Langmuir* **2010**, *26*, 2937−2944.

(18) Gao, W.; Wang, J. Synthetic micro/nanomotors in drug delivery. *Nanoscale* **2014**, *6*, 10486−10494.

(19) Wang, W.; Castro, L. A.; Hoyos, M.; Mallouk, T. E. Autonomous Motion of Metallic Microrods Propelled by Ultrasound. *ACS Nano* **2012**, *6*, 6122−6132.
(20) Garcia-Gradilla, V.; Orozco, J.; Sattayasamitsathit, S.; Soto, F.; Kuralay, F.; Pourazary, A.; Katzenberg, A.; Gao, W.; Shen, Y.; Wang, J. Functionalized Ultrasound-Propelled Magnetically Guided Nanomotors: Toward Practical Biomedical Applications. *ACS Nano* **2013**, *7*, 9232−9240.
(21) Gao, W.; Kagan, D.; Pak, O. S.; Clawson, C.; Campuzano, S.; Chuluun-Erdene, E.; Shipton, E.; Fullerton, E. E.; Zhang, L.; Lauga, E.; Wang, J. Cargo-Towing Fuel-Free Magnetic Nanoswimmers for Targeted Drug Delivery. *Small* **2012**, *8*, 460−467.
(22) Tierno, P.; Albalat, R.; Sagués, F. Autonomously Moving Catalytic Microellipsoids Dynamically Guided by External Magnetic Fields. *Small* **2010**, *6*, 1749−1752.
(23) Massana-Cid, H.; Martinez-Pedrero, F.; Navarro-Argemé, E.; Pagonabarraga, I.; Tierno, P. Propulsion and hydrodynamic particle transport of magnetically twisted colloidal ribbons. *New J. Phys.* **2017**, *19*, 103031.
(24) Xu, T.; Soto, F.; Gao, W.; Dong, R.; Garcia-Gradilla, V.; Magaña, E.; Zhang, X.; Wang, J. Reversible Swarming and Separation of Self-Propelled Chemically Powered Nanomotors under Acoustic Fields. *J. Am. Chem. Soc.* **2015**, *137*, 2163−2166.
(25) Zhou, C.; Zhang, H.; Li, Z.; Wang, W. Chemistry pumps: a review of chemically powered micropumps. *Lab Chip* **2016**, *16*, 1797−1811.
(26) Wong, F.; Sen, A. Progress toward Light-Harvesting Self-Electrophoretic Motors: Highly Efficient Bimetallic Nanomotors and Micropumps in Halogen Media. *ACS Nano* **2016**, *10*, 7172−7179.
(27) Das, S.; Shklyaev, O. E.; Altemose, A.; Shum, H.; Ortiz-Rivera, I.; Valdez, L.; Mallouk, T. E.; Balazs, A. C.; Sen, A. Harnessing catalytic pumps for directional delivery of microparticles in microchambers. *Nat. Commun.* **2017**, *8*, 14384.
(28) Sengupta, S.; Patra, D.; Ortiz-Rivera, I.; Agrawal, A.; Shklyaev, S.; Dey, K. K.; Córdova-Figueroa, U.; Mallouk, T. E.; Sen, A. Self-powered enzyme micropumps. *Nat. Chem.* **2014**, *6*, 415−422.
(29) Laskar, A.; Shklyaev, O. E.; Balazs, A. C. Controlling the Spatiotemporal Transport of Particles in Fluid-Filled Microchambers. *Langmuir* **2020**, *36*, 7124−7132.
(30) Donner, J. S.; Baffou, G.; McCloskey, D.; Quidant, R. Plasmon-Assisted Optofluidics. *ACS Nano* **2011**, *5*, 5457−5462.
(31) Li, M.; Su, Y.; Zhang, H.; Dong, B. Light-powered direction-controlled micropump. *Nano Res.* **2017**, *11*, 1−12.
(32) Tansi, B. M.; Peris, M. L.; Shklyaev, O. E.; Balazs, A. C.; Sen, A. Organization of Particle Islands through Light-Powered Fluid Pumping. *Angew. Chem., Int. Ed.* **2019**, *58*, 2295−2299.
(33) Guo, Y.; Wang, D.; Li, J.; Sun, Y.; Li, M.; Zhang, H.; Duan, R.; Zhang, D.; Song, B.; Dong, B. A fuel-free polymer-based micropump with optically tunable pumping directions. *J. Mater. Chem. C* **2019**, *7*, 2299−2304.
(34) Manna, R. K.; Shklyaev, O. E.; Kauffman, J.; Tansi, B.; Sen, A.; Balazs, A. C. Light-Induced Convective Segregation of Different Sized Microparticles. *ACS Appl. Mater. Interfaces* **2019**, *11*, 18004−18012.
(35) Peskin, C. S. The immersed boundary method. *Acta Numerica* **2002**, *11*, 479−517.
(36) Lim, S.; Ferent, A.; Wang, X. S.; Peskin, C. S. Dynamics of a Closed Rod with Twist and Bend in Fluid. *SIAM J. Sci. Comput.* **2008**, *31*, 273−302.
(37) Qian, Y. H.; D'Humières, D.; Lallemand, P. Lattice BGK Models for Navier-Stokes Equation. *Europhys. Lett.* **1992**, *17*, 479−484.
(38) Wang, Y.; Hernandez, R. M.; Bartlett, D. J.; Bingham, J. M.; Kline, T. R.; Sen, A.; Mallouk, T. E. Bipolar Electrochemical Mechanism for the Propulsion of Catalytic Nanomotors in Hydrogen Peroxide Solutions. *Langmuir* **2006**, *22*, 10451−10456.
(39) Baker, R.; Kauffman, J. E.; Laskar, A.; Shklyaev, O. E.; Potomkin, M.; Dominguez-Rubio, L.; Shum, H.; Cruz-Rivera, Y.; Aranson, I. S.; Balazs, A. C.; Sen, A. Fight the flow: the role of shear in artificial rheotaxis for individual and collective motion. *Nanoscale* **2019**, *11*, 10944−10951.

https://dx.doi.org/10.1021/acs.langmuir.0c00972
Langmuir 2020, 36, 10022−10032